Bulletin of Volcanology (2019) 81: 72
https://doi.org/10.1007/s00445-019-1333-6

RESEARCH ARTICLE

Petrology of the 2016–2017 eruption of Bogoslof Island, Alaska

Matthew W. Loewen[1] · Pavel Izbekov[2] · Jamshid Moshrefzadeh[2] · Michelle Coombs[1] · Jessica Larsen[2] · Nathan Graham[2] · Michelle Harbin[3] · Christopher Waythomas[1] · Kristi Wallace[1]

Received: 8 April 2019 / Accepted: 22 October 2019 / Published online: 28 November 2019

Abstract

The 2016–2017 eruption of Bogoslof primarily produced crystal-rich amphibole basalts. The dominant juvenile tephra were highly microlitic with diktytaxitic vesicles, and amphiboles had large reaction rims. Both observations support a magma history of slow ascent and/or shallow stalling prior to eruption. Plagioclase-amphibole-clinopyroxene mineralogy are also suggestive of shallow magma crystallization. Lavas were emplaced as shallow submarine lava domes and cryptodomes that produced 70 relatively short-lived and water-rich explosions over the course of the 9-month-long eruption. The explosions ejected older trachyandesite lavas that were likely uplifted by cryptodome emplacement that began in December 2016 and continued for many months. Trachyte pumice, similar in composition to a 1796 lava dome, was entrained in basalts by the end of the eruption. The pumice appears to be a largely crystalline magma that was rejuvenated, entrained in the basalt, and heated to ~ 1000 °C. The composition of trachytes require differentiation through stronger amphibole control than the apparent shallow crustal evolution implied for the basalt. This suggests that they are magmas derived from a mid-crustal zone of amphibole crystallization. Nearby arc-front volcanoes that notably lack amphibole have strikingly similar compositional trends. Trace element signatures of the Bogoslof basalts, however, suggest derivation from a mantle source with residual garnet and lower-degree melting than basalts from nearby arc-front volcanoes. The diversity of magmas erupted at Bogoslof thus provides an opportunity not only to probe rare backarc compositions from the Aleutian arc but also to examine the apparent role of amphibole in generating evolved compositions more broadly in arc environments.

Keywords Backarc · Lava domes · Surtseyan eruptions · Amphibole basalt · Trachyte

Editorial responsibility: J.J. Lyons;
Special Issue Editor: N. Fournier

This paper constitutes part of a topical collection:

The 2016-17 shallow submarine eruption of Bogoslof volcano, Alaska

Electronic supplementary material The online version of this article (https://doi.org/10.1007/s00445-019-1333-6) contains supplementary material, which is available to authorized users.

✉ Matthew W. Loewen
mloewen@usgs.gov

[1] U.S. Geological Survey, Alaska Volcano Observatory, Anchorage, AK, USA

[2] University of Alaska Fairbanks, Alaska Volcano Observatory, Fairbanks, AK, USA

[3] University of Alaska Fairbanks, Alaska Satellite Facility, Fairbanks, AK, USA

Introduction

Bogoslof volcano, an emergent stratovolcano located about 50 km behind the central Aleutian arc front, erupted from December 2016 to August 2017 in a series of 70 explosions and at least two dome building events (Fig. 1; Coombs et al. 2019; Waythomas et al. 2019a). Historically, Bogoslof is one of the more active Aleutian volcanoes with at least nine documented eruptions since 1796 (Waythomas and Cameron 2018). The most recent eruption prior to 2016 was effusion of a basaltic lava dome in 1992.

Only two detailed petrologic studies exist for Bogoslof: Byers (1961) provided a petrographic and geochemical survey of the 1926 and 1796 Bogoslof lava domes in an overview study that also included the nearby Unmak Island arc front volcanoes, and Arculus et al. (1977) provided a more focused study and added additional analyses of the 1883 lava dome. These studies showed that Bogoslof lavas were alkali-rich amphibole basalts to trachyandesites.

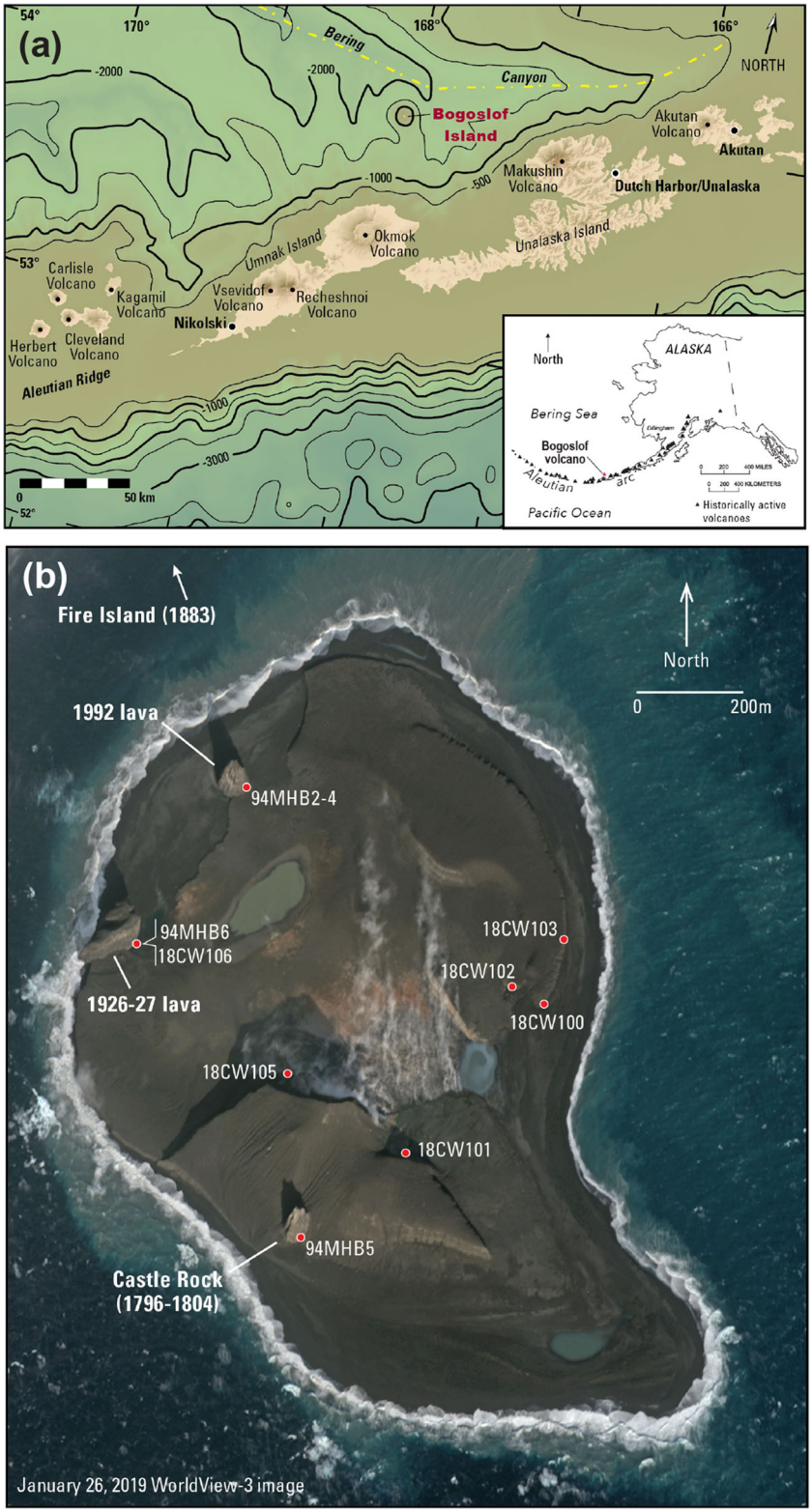

Fig. 1 **a** Location of Bogoslof Island in the southern Bering Sea. Major volcanoes of the central Aleutian arc also shown. Bathymetric contour interval is 500 m. Bathymetric data from the GEBCO 2019 Grid, a global terrain model of land and ocean; spatial resolution is 15 arc sec. **b** Worldview 3 satellite image from January 26, 2019 showing the island's configuration after the eruption, with sample locations show in red circles

Amphibole-bearing basalts rarely erupt. Other occurrences include Kick'em Jenny in the Lesser Antilles (Sigurdsson and Shepherd 1974), Mount Lamington in Papua New Guinea (Arculus et al. 1983), Cerro la Pilita in Western Mexico (Luhr and Carmichael 1985; Barclay and Carmichael 2004), and Buldir Island in the far western Aleutians (Waters et al. 2017). Despite their scarcity, amphibole plays an apparent role in early geochemical evolution of many arc rocks (Davidson et al. 2007, 2013).

Bogoslof is also one of only two subaerial volcanoes in the Aleutian Islands located significantly behind the main axis of volcanic vents. Amak Island, the other backarc center, has erupted basalts that are more typical of Aleutian arc tholeiites, with plagioclase, pyroxenes, and Fe-Ti oxides, and notable absence of amphibole (Marsh and Leitz 1978). The composition of lavas erupted from these two centers provide the only insight into the subarc mantle in the Aleutians from locations with greater slab depths.

The remote setting and wilderness designation of Bogoslof Island challenged monitoring during the 2016–2017 eruption (Coombs et al. 2018). Tephra samples were only collected on three occasions: when ash fell on the distant communities Nikolski and Dutch Harbor in the Aleutian Islands, and when ash fell on a boat off Cape Kovrizhka (Fig. 1). No proximal samples were collected until a year after the eruption ended. Despite this, remote seismic monitoring from nearby Unmak and Unalaska Islands (Tepp et al. 2019; Searcy and Power 2019), infrasound (Lyons et al. 2019a), lightning (Van Eaton et al. 2019), satellite (Lopez et al. 2019; Schneider et al. 2019), and rare direct observations were pieced together to detect explosive events, providing some insight on the mechanisms of eruption (Wech et al. 2018; Lyons et al. 2019b).

In this paper, we describe the texture, petrology, and geochemistry of the available physical products erupted during the 2016–2017 Bogoslof eruption, including samples of distal tephras from three explosive events and proximal samples collected in August 2018 after the conclusion of the eruption. These proximal samples were only collected from the surface of the island and likely represent the final phase of the eruption. We also report compositions for samples from 1992 and other historical eruptions collected during a visit to the island in 1994 but unpublished until now. The unusual eruption of an amphibole-bearing basalt provides important insight into potentially more ubiquitous but hidden magmatic processes in arcs globally.

Methods

Sample collection

Ash samples were collected from deposits of three explosive events during the eruption: event 29 (January 31), event 37 (March 8), and event 39 (May 17). January 31 samples were collected both shortly after deposition by community members in Dutch Harbor, Alaska, 100 km east of Bogoslof and in mid-February by Alaska Volcano Observatory geologists who were mapping the deposit across Unalaska Island. Samples of March 8 ashfall were collected immediately after deposition on a boat working offshore of Cape Kovrizhka, 60 km east of Bogoslof. A single May 17 ashfall sample was collected by a community member after deposition in Nikolski, Alaska, 120 km SW of Bogoslof. Splits of these tephra samples were wet-sieved and ultrasonicated before mounting in epoxy and polishing for analysis. Tephra componentry was described by counting > 500 grains from a mount of the 63–125 μm size fraction for all samples, and for ~ 80 grains from the coarse 125–250 μm size fraction available from the January 31 and March 8 samples. Criteria for tephra componentry is described in the online Supplementary Material. Sample locations, descriptions, and other metadata are also provided in the online Supplementary Material.

Eleven samples from the 1992, 1926, and 1796 "Castle Rock" lava domes (unit descriptions in Waythomas et al. (2019b) were sampled by Michelle Harbin during her 1994 field campaign.

Fifty-four samples were collected during two field days supported by the R/V Tiglax on August 15–16, 2018. All samples were described (see online Supplementary Material) and 33 were selected for bulk whole rock analysis. Polished petrographic thin sections were prepared for 12 representative samples and used for modal point-counting (n = 1500) and electron microprobe analysis.

In addition to lava samples, eight bulk tephra samples were collected from sections along wave-cut terraces on the island. One of these, 18CW100-4, was processed in a similar manner to distal ash samples. Plagioclase, amphibole, and clinopyroxene were hand-picked from the 125–250 μm size fraction of this sample and polished halfway through grains. Exposed melt inclusions were then identified in back-scatter electron images (BSE). All sample metadata are given in the online Supplementary Material.

Analytical methods

Polished grain mounts of tephra and petrographic thin sections of representative on-island samples were imaged using a JEOL 3510LV scanning electron microscope at the U.S. Geological Survey in Anchorage, AK. Images were obtained at high vacuum with an accelerating voltage of 15 kV, spot size (~ beam current) of 65, and a 12 mm working distance.

Quantitative analyses for glass and minerals were conducted at the University of Alaska Fairbanks Advanced Instrumentation Laboratory on a JEOL JXA8530F electron microprobe. Samples were carbon-coated to a thickness of ca. 250 Å. Details about beam conditions for glass and mineral analyses, spectrometer count times, calibration standards, and typical analytical uncertainties, are summarized in the online Supplementary Material.

Whole-rock compositions of 29 volcanic bombs and lavas along with chips of two mafic and two silicic inclusions, all collected on Bogoslof Island in August 2018, were analyzed at the Peter Hooper GeoAnalytical Laboratory of the Washington State University using X-ray fluorescence and ICP-MS analysis. Analytical procedure and uncertainties are discussed in Johnson et al. (1999) and in technical notes

posted at https://environment.wsu.edu/facilities/geoanalytical-lab/technical-notes/. Samples 18CW100-10B and 18CW103-4 were analyzed twice to demonstrate analytical reproducibility. An additional ten samples were analyzed, also at Washington State University, from a 1994 field expedition and included eight samples from the 1992 lava dome, one from the 1926 dome, and one from the 1796 dome.

Results

Erupted lithologies

Proximal products of the 2016–2017 Bogoslof eruption can be categorized into three major types: (1) basaltic scoria, (2) light-colored pumice, and (3) dense crystalline lavas exposed in an uplifted area emplaced as early as December 2016 (Fig. 2). The texture and mineralogy of these generalized lithologies are listed below, along with prominent inclusions of mafic and silicic material.

Basaltic scoria and dense blocks were the dominant clast type found on the surface of the island in 2018. They range in size from lapilli to large 2 m bombs and in density from dense to highly vesicular scoria. All are dark in color with 1–2 mm plagioclase and amphibole phenocrysts visible in hand-sample. Modes of typical samples are 30–40% plagioclase, 10–15% clinopyroxene, 3–10% amphibole, and 3–6% Fe-Ti oxides (calculated as vesicle-free). The remaining 35–45% of material is variably microlitic groundmass of glass, plagioclase, clinopyroxene, Fe-Ti oxides, orthopyroxene, and rounded olivine (Fig. 2a, Table 1).

Bombs of light-colored pumice were concentrated around the main vent, ranged to 0.5 m in diameter, and made up less than 5% of the observed surface cover. Many of these pumice clasts are coated in a glassy rind of basalt (Fig. 2b) and some are apparent as mingled pumice bands in basalt scoria. Visible phenocrysts in hand-samples include plagioclase, pyroxene, and small unidentified mafic minerals. The pumices have around 60% vesicularity. The vesicle-free mode is 11% microlite-free glass, 61% plagioclase, 9% Fe-Ti oxides, 5% sanidine, 5% amphibole pseudomorphs, 4% clinopyroxene, and 4% biotite, with trace quartz and titanite.

Dense, somewhat altered lava blocks were sampled from a talus pile at the base of a ~ 100 m tall, east-facing outcrop near the main 2016–2017 eruptive vent. This face is on the eastern side of a feature that was shown by retrospective analysis of satellite data to have initially uplifted in December 2016 (Coombs et al. 2019; Waythomas et al. 2019a). An absence of increased thermal output during the period of uplift (Coombs et al. 2019) suggest that this feature is not a dome of juvenile 2016–2017 magma, but instead perhaps the roof above a shallow cryptodome. The outcrop had pervasive hydrothermal alteration and samples were selected from less altered zones. These samples have a light-colored groundmass with visible phenocrysts of 2 mm plagioclase and pyroxene, and up to 10 mm—but typically 1 mm—amphibole. The amphibole proportion estimated in hand sample was variable from ~ 1% to almost 15%. Modes of two samples are 25–50% plagioclase, 3–10% clinopyroxene, 3–10% amphibole, 2–4% Fe-Ti oxides, and trace apatite. Groundmass of sanidine and plagioclase microlites, an amorphous silica phase, and irregular void-space make up the remaining 30–60% of the samples (Fig. 2c).

Basaltic scoria samples contain abundant mafic and silicic inclusions (Fig. 2d, e, f). Quenched mafic inclusions are vesicular with microlite-free glass and an identical plagioclase-pyroxene-amphibole phenocryst assemblage to host basalt (Fig. 2f). Coarse gabbroic inclusions are also common with biotite, amphibole, plagioclase, apatite, and calcite (BSE in Fig. 2e, also visible in hand sample in Fig. 2c). Light-colored silicic inclusions are less common, but conspicuous. These include dense to frothy vesicular and microvesicular material with a subtle layering of light and darker colors, reminiscent of a sedimentary rock, but no hand-sample visible phenocrysts (Fig. 2d). Small rounded quartz and orthopyroxene phenocrysts are found in BSE imaging.

Tephra componentry

Samples of the January 31, March 8, and May 17 ashfalls include (1) free crystals of plagioclase, clinopyroxene, amphibole, Fe-Ti oxides, and rare biotite; (2) microlitic to glassy juvenile grains with groundmass textures similar to basalts collected on the island (Fig. 3a, b); and (3) variably altered material with sanidine microlites matching the uplifted dome lithologies collected proximally (Fig. 3c, d). No tephra grains matching the pumice textures or compositions were found in the three sampled explosive events, suggesting that they were either a very minor eruption component and/or a late product erupted primarily after May 17, 2017.

Componentry of the 63–125 μm size fraction is dominated by ~ 40% free crystals. Twenty percent are plagioclase while another 20% are undifferentiated amphibole and clinopyroxene. Two to three percent are Fe-Ti oxides (see online Supplementary Material). The crystal proportion at this size range is somewhat underestimated, as mostly crystalline fragments with adhered groundmass were classified by lithology, not as crystals. Thus, the overall crystallinity and phase proportions are reasonably similar to the basaltic lithology collected on-island.

Highly microlitic and diktytaxitic grains with plagioclase, clinopyroxene, Fe-Ti oxide, olivine, and minor glass dominate 55–70% the non-crystal fraction (Fig 3b). Similar mineralogy but higher glass proportions and rounded vesicles make up 10–15% of the grains, with most of these still moderately microlitic (Fig. 3a). The more microlitic grains can be highly vesicular to more compacted.

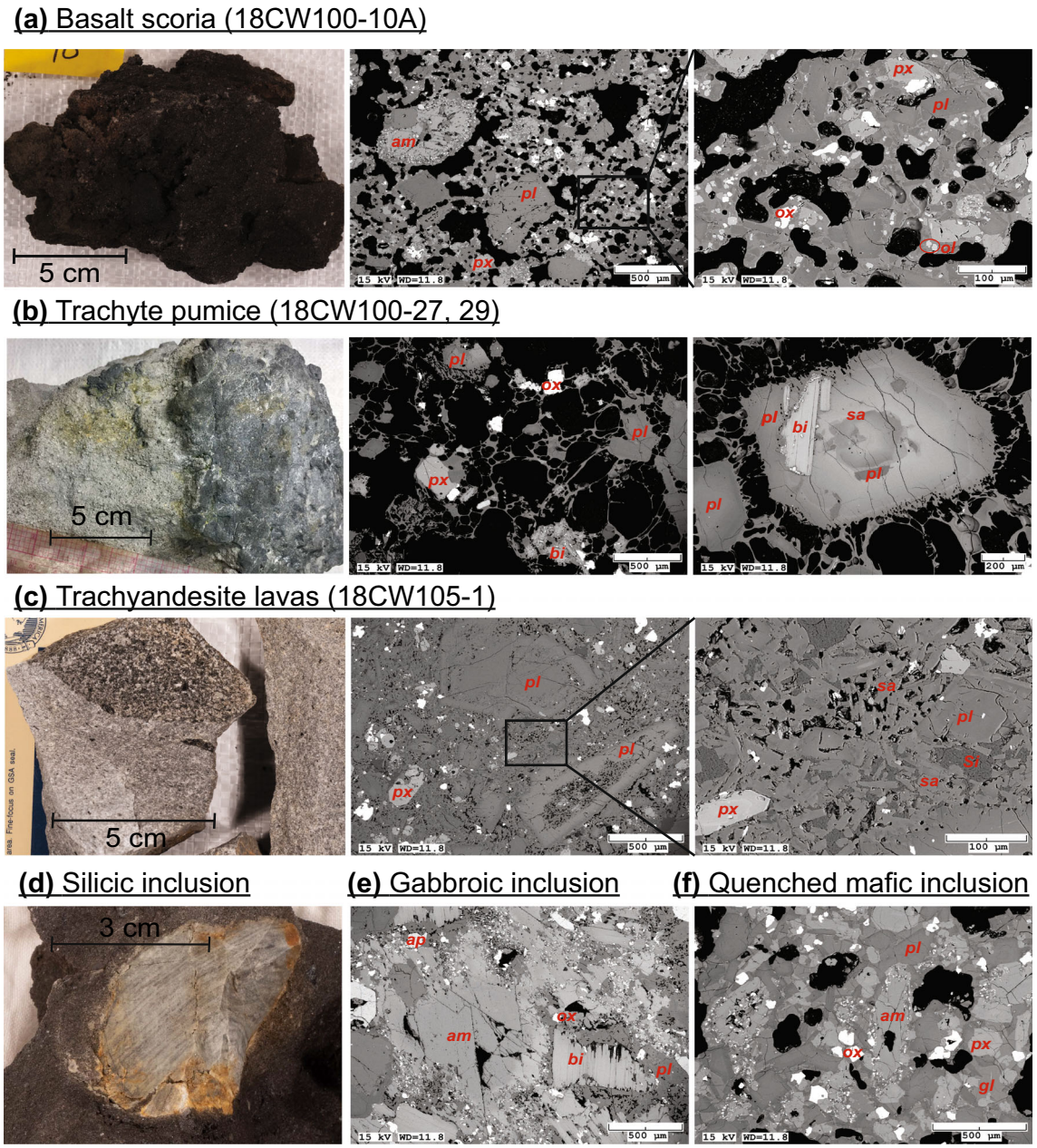

Fig. 2 Photographs (**a**, **b**, **c** left) and backscatter electron images (BSE, middle and right) of major lithologies erupted from the 2016–2017 eruption of Bogoslof sampled on the island in August 2018: **a** basalt scoria clasts, **b** white pumice blocks, and **c** uplifted dense dome-like rocks that form a topopgraphic rise first emplaced in December 2016. Bottom row of images are prominent examples of inclusions found in scoria and dome rocks including (**d**) photograph of a layered silicic inclusion, (**e**) BSE of a biotite-hornblende gabbro, and (**f**) a BSE of a glassy quenched mafic inclusion. Minerals identified on BSE images are abbreviated: amphibole (am), plagioclase (pl), clinopyroxene (px), Fe-Ti oxides (ox), olivine (ol), sanidine (sa), amorphous silica phase (Si), and biotite (bi)

Vesicle-free grains with a dense interlocking network of feldspar microlites, including sanidine, and sometimes alteration minerals including clays and pyrite, comprise 15–40% of the non-crystal fraction (Fig. 3c, d) likely correlating with the uplifted 2016–2017 lithologies (Fig. 2c). The proportion of these grain types decreased from almost 40% of the non-crystalline fragments on January 31 to less than 15% on May 17.

We also examined a smaller number of grains from the 125–250 µm size fraction of the January and March events as well as the proximal on-island sample that mineral separates were collected from for melt inclusion analysis (18CW100-4). No significant differences were seen in the proximal sample, suggesting it is broadly representative of the distal sample compositions.

Table 1 Representative bulk compositions from Bogoslof 2016–2017 eruption

Sample ID	18CW100-10A Scoria	18CW105-1A Dome	18CW100-27 Pumice	18CW100-13B Inclusion	18CW105-1B Inclusion
Modal observations (% vesicle/void-free)					
Vesicles/voids	18	0.1	58	17	0
Groundmass	45 (glass, plag, cpx, ox, ol)	34 (san, plag, Si, cpx, ox)	11 (glass)	12 (glass)	0
Phenocrysts	29 plag	50 plag	61 plag	56 plag	51 plag
	11 cpx	10 cpx	9 ox	18 cpx	18 cpx
	11 amph	4 ox	5 san	10 amph	15 bio
	4 ox	3 amph	5 amph[a]	5 ox	5 amph
		tr.apa	4 cpx		3 ox
			4 bio		1 calc
			tr. qtz, tit		tr. opx, apa
Major elements (wt%)					
SiO_2	49.98	59.13	60.27	48.70	48.71
TiO_2	1.22	0.64	0.56	1.30	1.31
Al_2O_3	17.95	18.74	19.51	17.94	16.75
FeO(t)	9.71	5.16	4.74	10.34	9.42
MnO	0.19	0.16	0.10	0.19	0.21
MgO	4.82	1.60	1.34	5.14	7.07
CaO	10.73	6.67	6.06	11.40	11.38
Na_2O	3.11	4.21	4.31	2.85	2.28
K_2O	1.91	3.41	2.89	1.75	2.57
P_2O_5	0.39	0.29	0.22	0.38	0.29
Sum	99.29	99.09	98.85	99.29	98.56
LOI	0.00	0.18	0.26	0.00	0.76
Trace elements (ppm)					
Sc	31	7.0	4.9	34	39
V	324	136	98	360	349
Cr	17	4.7	2.8	7.3	260
Ni	29	5	2	13	83
Cu	69	24	6	74	35
Zn	77	64	31	77	110
Ga	20	21	21	21	21
Rb	54	160	80	48	113
Sr	768	816	892	795	652
Y	23	23	23	22	18
Zr	121	258	264	112	114
Nb	3.6	8.9	7.2	3.3	4.8
Cs	1.9	3.5	0.78	1.7	3.1
Ba	901	1664	2400	839	1984
La	17	32	27	16	15
Ce	40	65	59	38	34
Pr	5.8	8.0	7.8	5.7	4.7
Nd	26	31	31	25	21
Sm	5.9	5.9	6.2	5.8	4.9
Eu	1.7	1.7	1.8	1.8	1.3
Gd	5.3	4.7	4.8	5.2	4.1
Tb	0.79	0.72	0.73	0.79	0.63
Dy	4.6	4.2	4.3	4.4	3.7
Ho	0.95	0.86	0.88	0.90	0.71

Table 1 (continued)

Sample ID	18CW100-10A Scoria	18CW105-1A Dome	18CW100-27 Pumice	18CW100-13B Inclusion	18CW105-1B Inclusion
Er	2.4	2.5	2.4	2.4	1.9
Tm	0.35	0.35	0.38	0.34	0.27
Yb	2.2	2.4	2.5	2.1	1.6
Lu	0.33	0.38	0.40	0.31	0.27
Hf	3.4	6.3	6.3	3.3	3.3
Ta	0.24	0.54	0.51	0.22	0.22
Pb	4.7	7.9	5.4	4.5	4.4
Th	4.0	15	9.7	3.4	2.1
U	1.7	6.5	4.3	1.5	0.88

Groundmass and phenocryst percentages calculated as vesicle-free. All point counts are based on $n = 1500$ over a standard petrographic thin section. Mineral abbreviations are plagioclase (plag), clinopyroxene (cpx), orthopyroxene (opx), Fe-Ti oxides (ox), amphibole (amph), olivine (ol), amorphous silica (Si), apatite (apa), biotite (bio), titanite (tit), quartz (qtz), and calcite (calc)

[a] Amphibole percentages include amphibole pseudomorphs, and no unaltered amphibole was found in 18CW100-7. Major elements and Sc, V, Cr, Ni, Cu, Zn, and Ga by XRF, other trace elements by ICP-MS. See online Supplementary Material for other sample data and analytical methods

Whole rock and glass geochemistry

Bulk compositions of samples collected on Bogoslof range from basalt to trachyte (48–67 wt% SiO_2; Fig. 4). The compositional trend forms a higher alkali series than Aleutian arc-front volcanoes such as nearby Okmok and Makushin, but overlaps compositions at Amak, the other backarc volcanic center to the east (Marsh and Leitz 1978; Fig. 1). Both Bogoslof and arc-front mafic to intermediate compositions are tholeiitic following Miyashiro's (1974) classification.

All 2016–2017 scoriaceous material is basalt to trachybasalt (48–51 wt% SiO_2[1]). These samples overlap with compositions of the 1926 and 1992 lava domes, although 1992 samples have compositions extending to slightly higher SiO_2 (~ 52 wt%, Fig. 4). A larger gabbroic and quenched vesicular mafic inclusion were separated for whole rock analysis and fall in the same general compositional range as the basaltic scoria. The gabbroic inclusion has > 0.5 wt% higher K_2O concentration and > 2× concentrations of Rb, Ba, and Cs than other basalts at the same SiO_2 concentration (Table 1, Figs. 5 and 6). All basalts have enriched REE concentrations, chondrite-normalized La/Yb = 5–6, and lack significant Eu anomalies (Fig. 7). Matrix glass was analyzed in both the quenched mafic inclusion and its host scoria. In both samples, the glass fraction is a more evolved trachyandesite with 60–63 wt% SiO_2 and higher K_2O concentrations than any whole rock compositions from Bogoslof (Fig. 5). Matrix glass in the more microlitic host glass is slightly more evolved (higher SiO_2, lower MgO), but notably has lower K_2O despite the apparent absence of K-bearing minerals in the groundmass.

[1] One sample, 18CW103-3, had lower SiO2 ~ 46 wt%, however, secondary mineral precipitates were noted on vesicle walls and the sample had a slightly lower analytical total < 98 wt%, suggesting possible alteration, thus, we do not include this sample in the compositional range.

Rocks exposed in the December 2017 uplifted area south of the main 2016–2017 vent are dense, dome-like tholeiitic trachyandesites (Fig. 4). These intermediate compositions have notably lower alkali (Na_2O, K_2O) and higher CaO concentrations than basaltic matrix glass at similar SiO_2 (Fig. 5). Trace element concentrations of Sr, Ga, and Y are similar to the basalts, Sc, V, Cr, Ni, Cu, Zn, and MREEs are lower than basalts, and Rb, Ba, LREEs, HREEs, and other high-field strength elements (e.g., Nb, Zr, U) are higher than the basalts (Table 1, Fig. 6). Like the basalts, trachyandesites lack Eu anomalies (Fig. 7).

Light-colored pumice clasts span compositions from trachyandesite to trachyte, and cross the tholeiitic-calc-alkaline divide (Fig. 4). The four analyzed pumice samples form a major element trend slightly offset from the dome rocks. Trace element trends almost all contrast basalt trends, with decreasing concentrations as SiO_2 increases. Eu anomalies remain largely absent (Figs. 6 and 7). MREE depletion is most pronounced in the pumices compared to basalts and dome rocks with a distinctive concave-up pattern typical of amphibole fractionation (Fig. 7). Matrix glass in the pumice is rhyolitic with 70–77 wt% SiO_2.

Whole rock analyses from two fine-grained silicic inclusions—a layered vesicular pumice and a layered microvesicular dense inclusion—have compositions significantly offset from the main magmatic products of Bogoslof with a dacite and low-K rhyolite composition (Fig. 4). Compatible oxide (e.g., CaO, FeO(t), MgO) concentrations are higher in these inclusions than would be expected in evolved volcanic rocks.

Tephra glass geochemistry

Matrix glass compositions overlap in the January 31, March 8, and May 17 tephra samples and range from 51

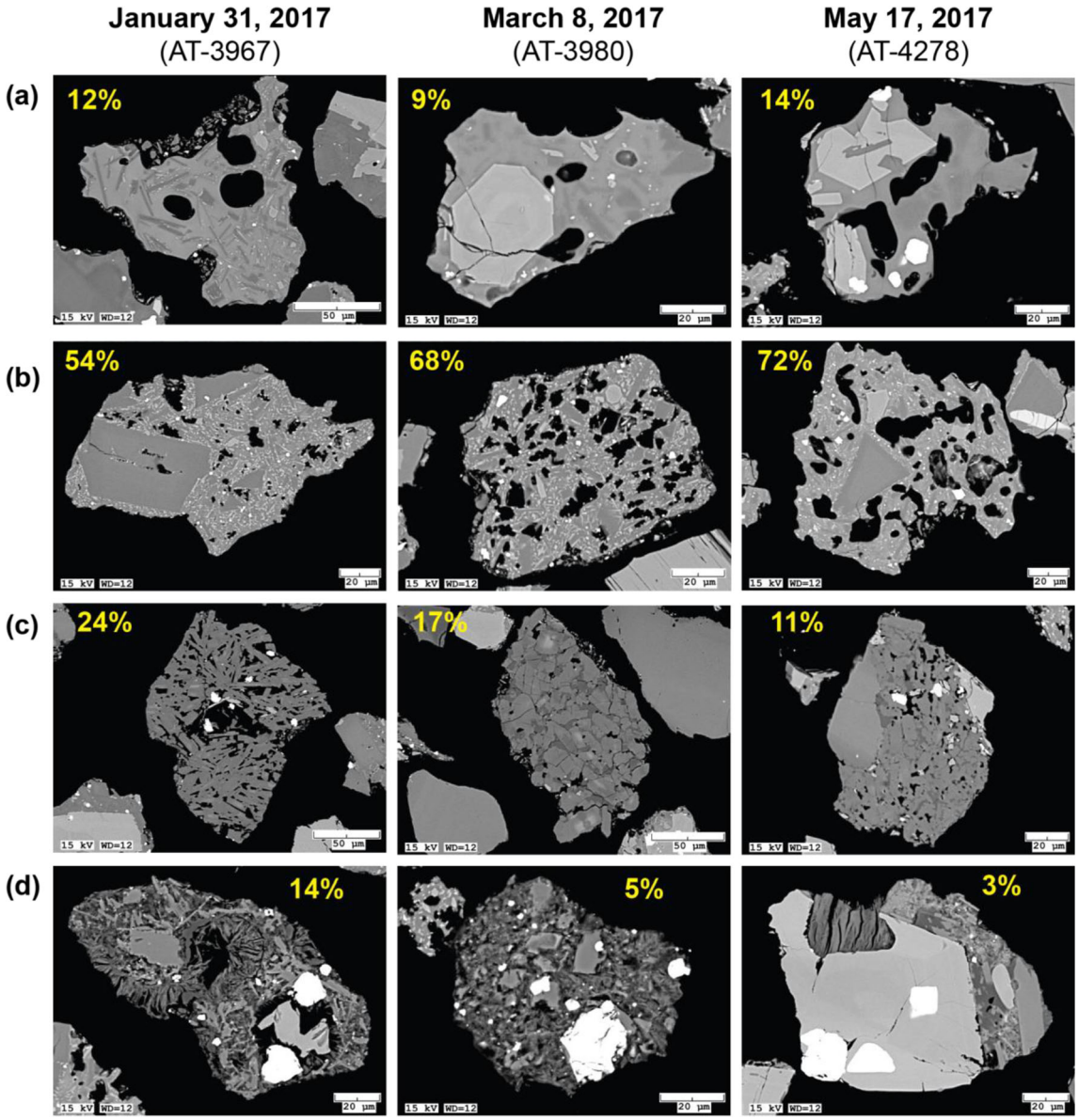

Fig. 3 BSE images of typical fragments in tephra collected from the January 31, March 8, and May 17, 2017 explosive events. Similar components are found in all samples: **a** glassy mafic scoria with slightly to moderately microlitic glass and rounded vesicles, **b** gradational variation from moderately to highly microlitic mafic scoria with diktytaxitic vesicles, **c** dense to porous crystalline grains with plagioclase and sanidine microlites and an interstitial SiO_2 phase (likely cristobalite), and **d** clay and sulfide alteration minerals typically associated with similar microlite mineralogy as (**c**). Percent of each component is shown in yellow, excluding ~ 40% of the total particles in each sample that are free crystals. Percentages based on count of $n = 500$ grains counted for each sample

to 67 wt% SiO_2 (Fig. 5). This compositional range includes analyses of rare microlite-free glass to highly microlitic melt residue (Fig. 3). Compositions trend towards and overlap with the matrix glass measured in the mafic enclave and its host from bulk rock samples (Fig. 5).

Melt inclusions

Amphibole-, clinopyroxene-, and plagioclase-hosted melt inclusions separated from the uppermost few meters of proximal pyroclastic deposits of the 2016–2017 eruption have glass compositions largely overlapping that of the distal tephra matrix glass (Fig. 8). Some plagioclase and clinopyroxene compositions are more evolved with lower K_2O than basalt matrix glasses, and these inclusions overlap the compositional range of the trachyte pumice. Chlorine concentrations in melt inclusions are actually lower on average than matrix glasses, but still higher than Cl in the evolved trachyte pumice. Sulfur concentrations, not measured in matrix glass, reach up to 3000 ppm, but are lower in the more evolved inclusions with > 60 wt% SiO_2, and are also lower in amphibole-hosted inclusions. Preliminary water concentrations of 1.9 and 2.9 wt%

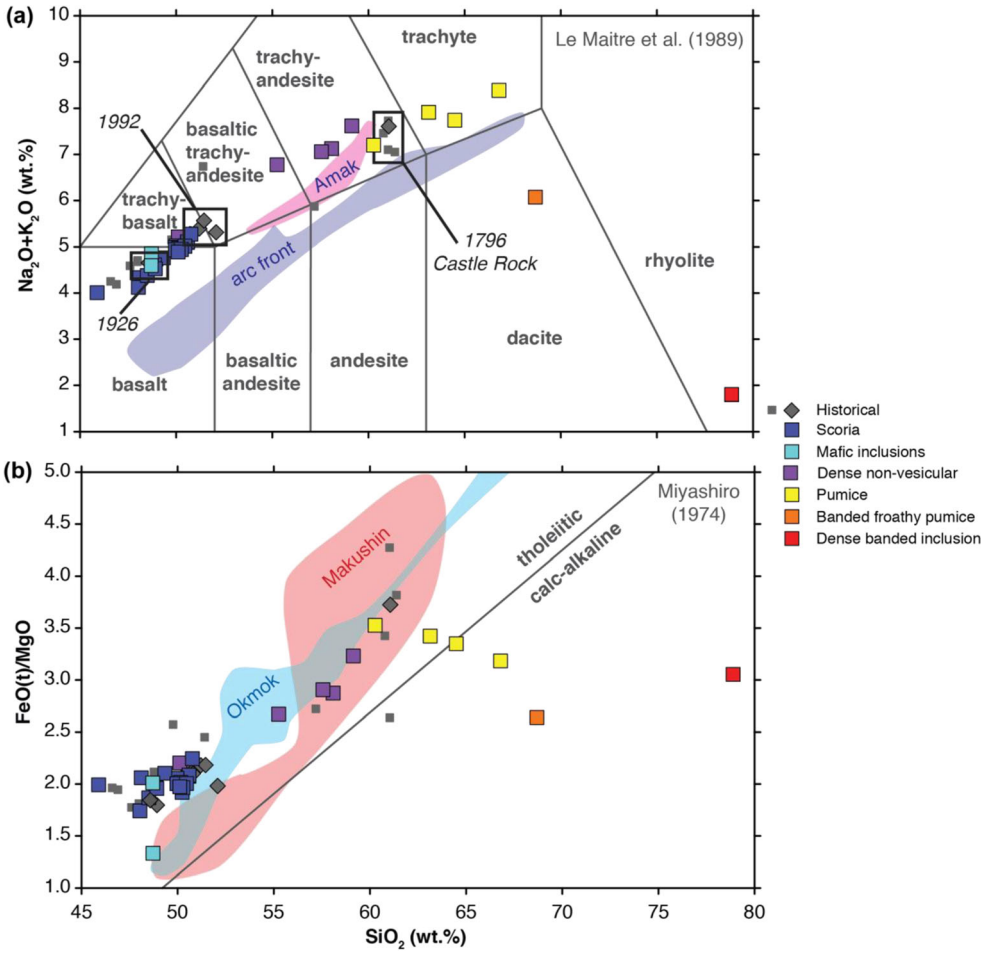

Fig. 4 **a** Total alkali vs. silica diagram of Le Maitre et al. (1989). Also shown are compositional fields for nearby arc-front volcanoes (Okmok, Makushin) and Amak, the other backarc center in the Central Aleutian arc (Okmok and Makushin data from Nye and Reid 1986; Nye et al. 1986; McConnell et al. 1998; Bean 1999; Finney et al. 2008; Nye et al. 2018; Amak data from Marsh and Leitz 1978; Yogodzinski et al. 2015). **b** Bogoslof as well as arc-front volcanoes in the Central Aleutians are tholeiitic in composition following Miyashiro (1974). Small gray square symbols are previously published data for Bogoslof (Byers 1961; Arculus et al. 1977)

in two plagioclase-hosted melt inclusions and 2.7, 3.2, and 3.2 wt% in three clinopyroxene-hosted melt inclusions were determined by attenuated total reflectance FTIR (Lowenstern and Pitcher 2013). This method, however, is only calibrated for calc-alkaline glass compositions, and thus these results are only a preliminary estimate of potential pre-eruptive water concentrations.

Mineral compositions

Basalts

Plagioclase is the most abundant mineral phase in the proximal basalts. It occurs as phenocrysts, microphenocrysts, and microlites. Plagioclase composition ranges from 47 to 92 mol% anorthite (An, mol%). A typical plagioclase phenocryst has an anhedral, sometimes sieved An_{82} core. The dissolution boundary between the core and the outer portion of the phenocryst marks an increase An_{82} to about An_{90}, followed by a zone of relatively constant composition, which oscillates between An_{83} and An_{88}. This zone is followed by a euhedral textural boundary where composition of the plagioclase drops abruptly from An_{88} to An_{81}, after which it exhibits continuous rim-ward increase until reaching An_{82}. Lastly, the anorthite content decreases from An_{82} to An_{48} over approximately 30 μm (Fig. 9a). Plagioclase microlites have bimodal compositions. One mode is characterized by an average of An_{67} overlapping phenocryst rim compositions. The second mode is characterized by approximately An_{83}.

Clinopyroxene occurs as euhedral phenocrysts, microphenocrysts, and microlites. The composition of clinopyroxenes ranges from 31 to 45 mol% enstatite (En, mol%). Large phenocrysts commonly contain resorbed cores made of either amphibole or En_{33} clinopyroxene. Resorbed amphibole cores are often surrounded by poikilitic inclusions of magnetite and microlite-rich melt inclusions. Composition of the clinopyroxene rims is relatively constant at En_{41}, occasionally exhibiting subtle normal zoning with core-to-rim compositions from En_{40} to En_{37}. Clinopyroxene microlites are En_{40-42} consistent with phenocryst rims (Fig. 10a).

Amphiboles occur as phenocrysts and are all surrounded by relatively large 40–100 μm wide reaction rims. Larger phenocrysts contain anhedral cores characterized by 11–12 wt% MgO and 13–15 wt% FeOt (Fig. 11a). The cores are separated from the rims by a dissolution

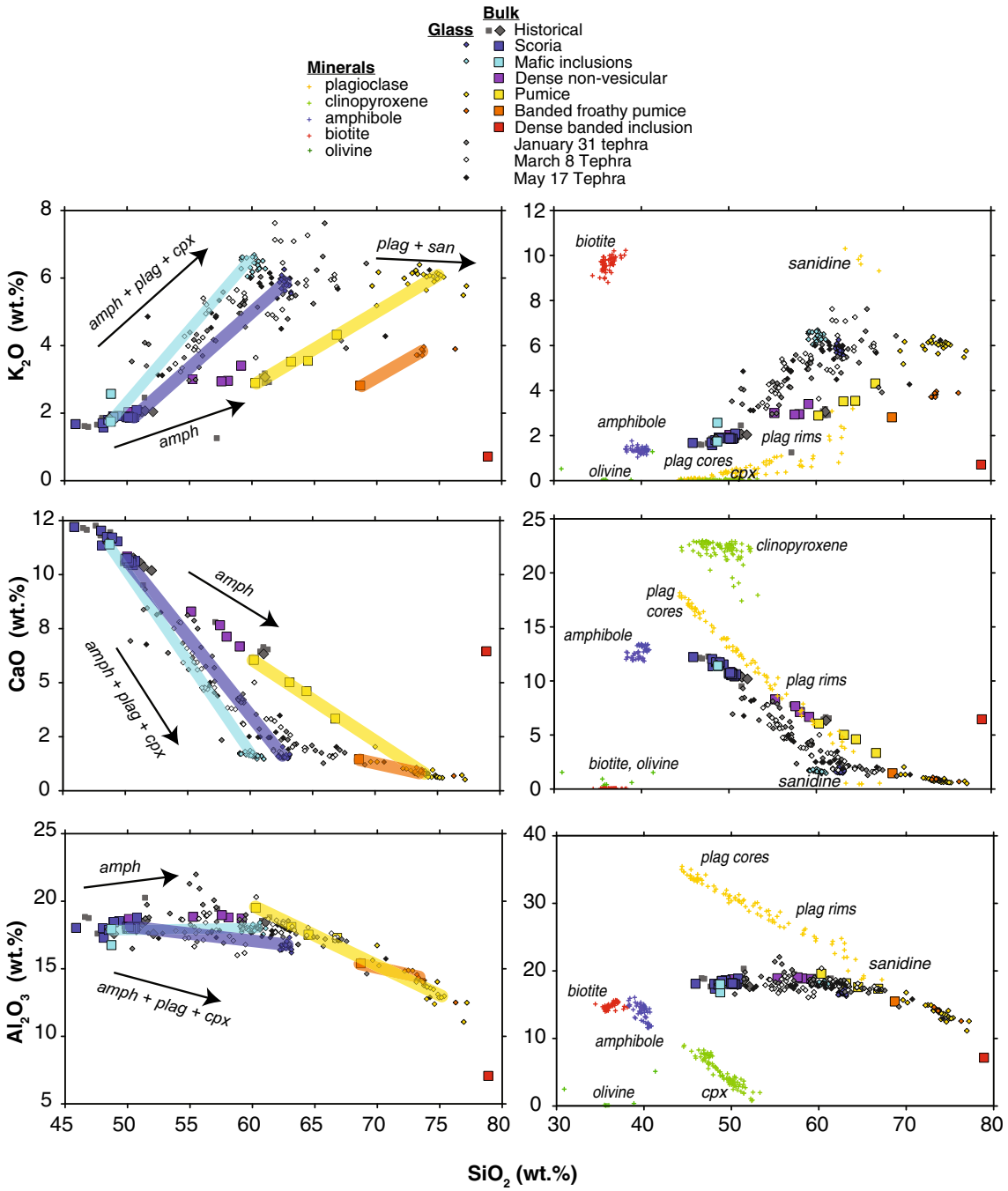

Fig. 5 Major element Harker diagrams with whole rock and matrix glass compositions (left). Expanded plots with measured mineral compositions (right). Generalized vectors for amphibole control and observed shallow amphibole + plagioclase + clinopyroxene crystallization are annotated on the left. Abbreviations used: amphibole (amph), plagioclase (plag), clinopyroxene (cpx), and sanidine (san). Sanidine and biotite are only found in the trachyte pumice, while olivine is only a microlite phase in basalts. Additional Harker diagrams for TiO_2, FeO(t), MgO, and Na_2O are available in the online Supplementary Material

boundary. Composition of the rims is characterized by 13.5–14 wt% MgO and 10–11 wt% FeO(t). The composition of rims is homogenous and the same across phenocrysts, whereas the composition of individual cores is homogenous but variable between different phenocrysts.

Olivine is present exclusively as microlites and rare microphenocrysts with approximately 64 mol.% of forsterite content. Similar to olivine, orthopyroxene also occurs only as microlites. Their composition is bimodal with one mode characterized by approximately En_{53} and the other by En_{66}.

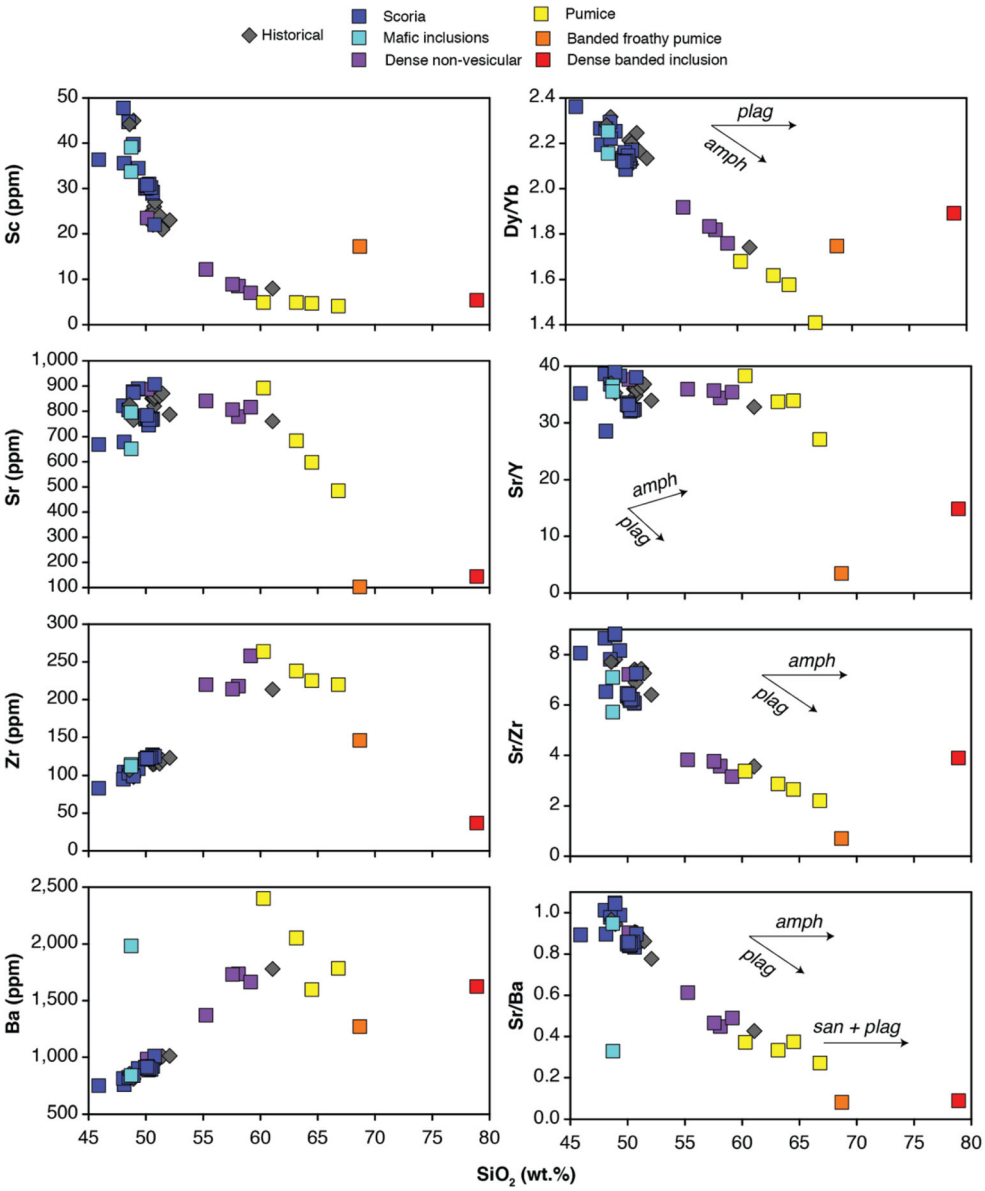

Fig. 6 Trace element and trace element ratio Harker diagrams. Illustrative vectors for mineral-specific fractionations are shown on ratio plots

Trachyandesites

Two populations of plagioclase phenocrysts are present in uplifted trachyandesites. (1) Normally zoned cores with compositions from An_{58} to An_{44}, followed by an anhedral dissolution boundary is accompanied by a slight increase in anorthite content to An_{48}. This rise in anorthite content is then followed by a steep and continuous decrease from An_{48} to An_{28}. (2) Subhedral $An_{79–87}$ cores with $An_{40–61}$ rims (Fig. 9b). Rim compositions of both plagioclase compositions are similar, and more sodic than basalt rims consistent with a more evolved bulk rock composition. Plagioclase core compositions overlap with basalt plagioclase phenocrysts.

Most clinopyroxene phenocrysts have En_{36} cores, with one to two dissolution surfaces, at which enstatite content decreases to En_{33}. Less commonly, clinopyroxene phenocrysts contain subhedral En_{40} cores. The En_{40} core composition overlaps with basalt clinopyroxene compositions (Fig. 10b).

Amphibole occurs as euhedral phenocrysts both with and without reaction rims. Phenocrysts contain anhedral cores characterized by 11–13 wt% MgO and 11–15 wt% FeO(t). The boundary between core and rim seems to be euhedral, and the rim is characterized by 10.2–10.4 wt% MgO and 14–18 wt% FeO(t) (Fig. 11b). The composition of amphibole phenocrysts is highly heterogeneous.

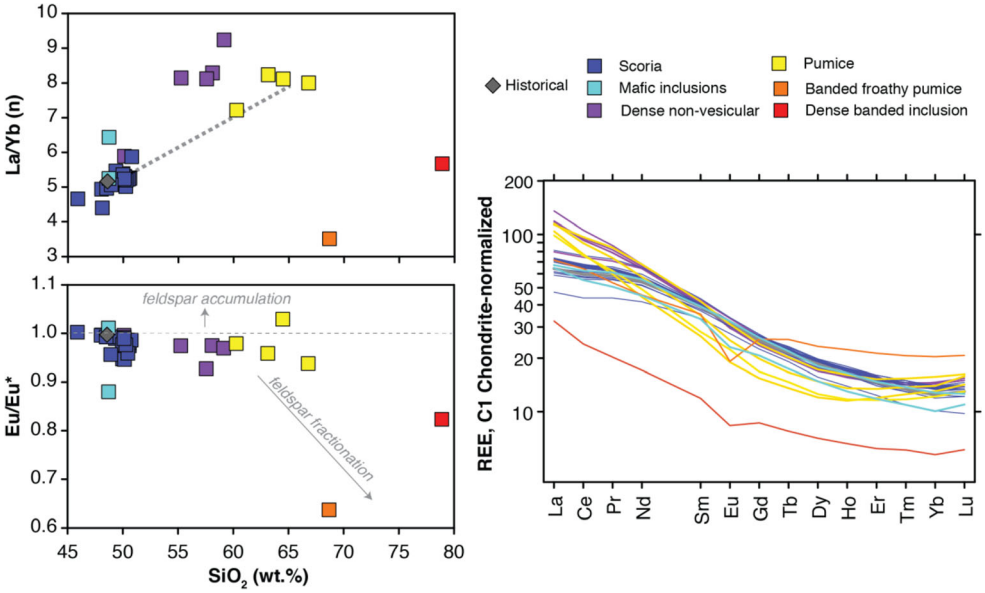

Fig. 7 Rare earth element (REE) plots. Light REEs increase from basalts to trachytes resulting in higher La/Yb. Middle REEs are depleted in more evolved trachytes reflected in Dy/Yb (see Fig. 6). Europium anomalies are largely absent in whole rock compositions

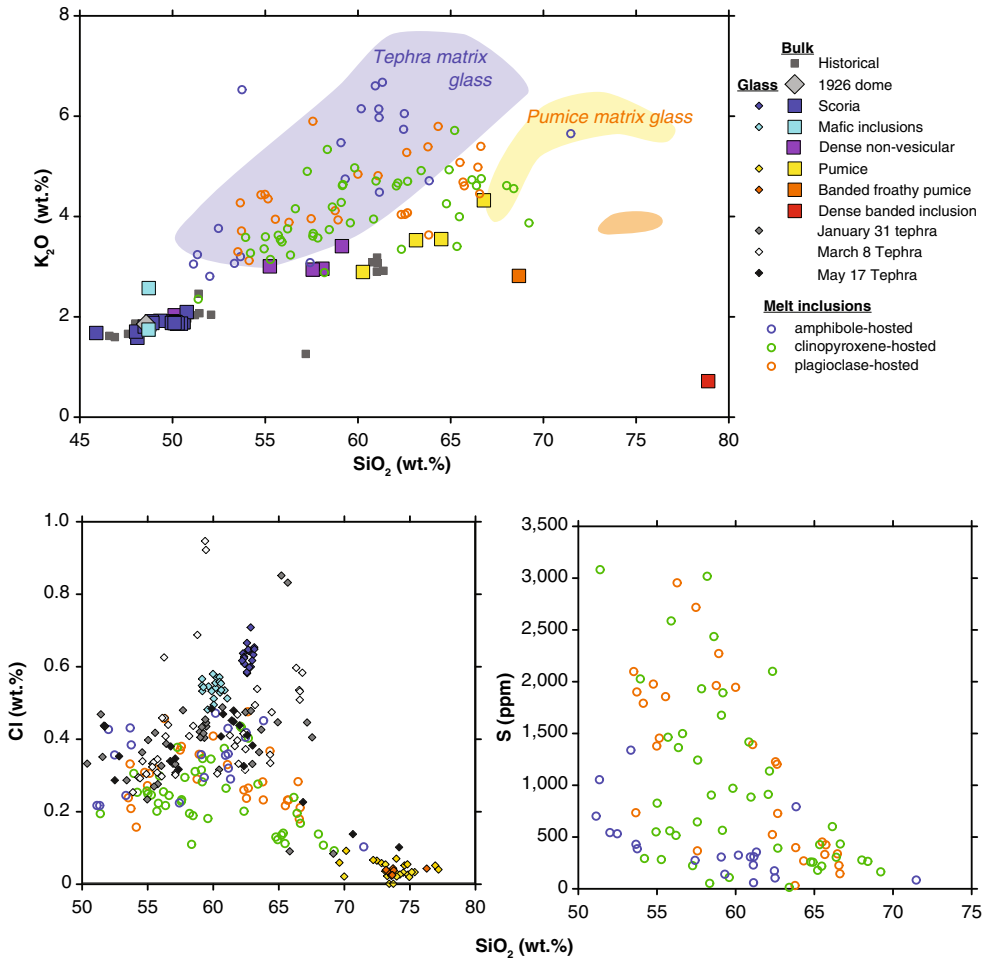

Fig. 8 Melt inclusion compositions overlap matrix glass compositional ranges (shown in background shading, see Fig. 5 for data). Chlorine concentrations are higher in matrix glass than melt inclusions. Sulfur values in melt inclusions reach 3000 ppm

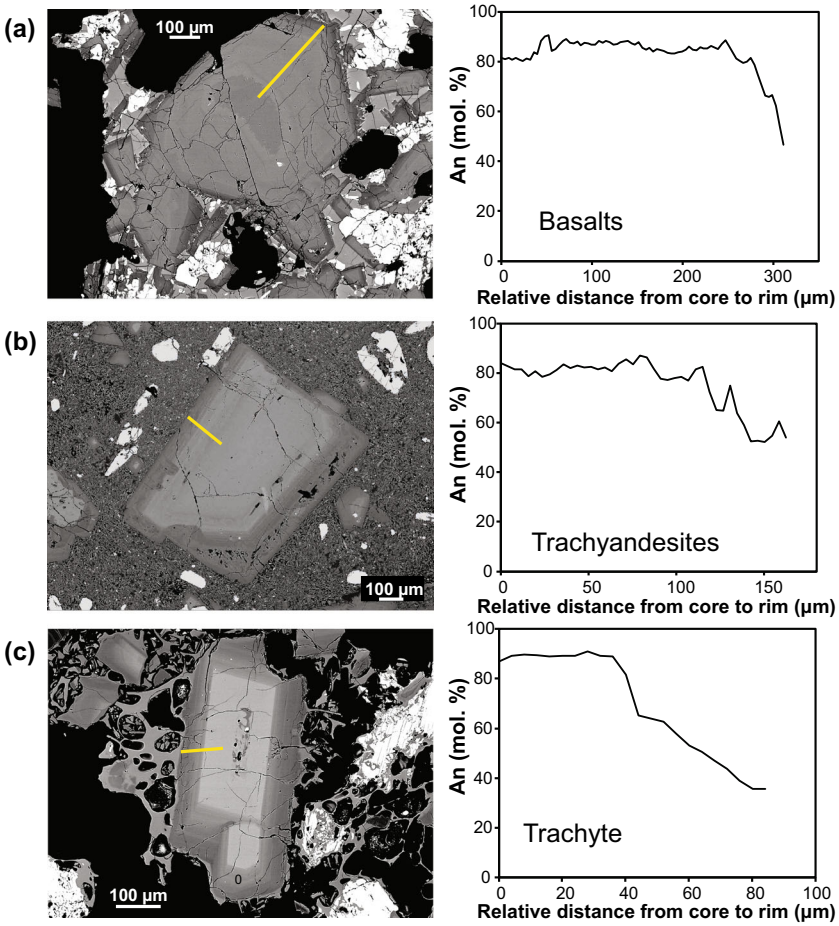

Fig. 9 BSE images and corresponding EPMA transects for representative plagioclase phenocrysts from **a** basalts, **b** trachyandesites, and **c** trachytes.

Trachyte pumice

Two populations of plagioclase phenocrysts are present in the trachyte pumice. (1) Oscillatory-zoned phenocrysts with An_{65} to An_{29} compositions, with the compositions gradually changing to more sodic values near the rim. (2) Phenocrysts with euhedral $An_{82–91}$ cores surrounded by oscillatory-zoned $An_{35–58}$ rims (Fig. 9c). Both populations have similar rim compositions but only the core composition of the second type match the 2016–2017 basalt.

Clinopyroxene phenocrysts in light pumice exhibit relatively constant composition. Starting with an En_{37} core with oscillatory variations towards the rim between En_{36} and En_{38} (Fig. 10c). This composition overlaps considerably with clinopyroxene phenocrysts from the trachyandesite. Although amphibole phenocrysts are absent in the pumice, there are abundant opaque pseudomorphs of amphibole (Fig. 11c). Orthopyroxene is present in light pumice as En_{69} microlites.

Biotite occurs in pumices as euhedral to subhedral 0.4–1.0 mm-long tabular phenocrysts, as well as microlites. Their compositions appear to be homogeneous and nearly constant across crystals with 13.8–18.1 wt% FeO(t), 12.7–14.1 wt% MgO, 3.7–4.3 wt% TiO_2, and 0.18–0.35 wt% MnO. Composition of biotite in light pumices is conspicuously different from the composition of accidental biotite grains found in the January 31, 2017 volcanic ash deposits (see online Supplementary Material).

Fe-Ti oxides in pumice include both titanomagnetite and ilmenite. Composition of six magnetite-ilmenite pairs were measured as 0.25–0.27 ulvospinel and 0.72–0.75 magnetite for titanomagnetite, and 0.57–0.63 ulvospinel and 0.37–0.43 magnetite for ilmenite (see online Supplementary Data). The pairs appear to be in equilibrium according to the Mn/Mg test of Bacon and Hirschmann (1988). Based on the revised calibration of the ilmenite–magnetite geothermometer by Ghiorso and Evans (2008), the pre-eruptive temperature and oxygen fugacity of trachyte pumices ranged from 977 to 1056 °C and from NNO+1.27 to NNO+1.65, correspondingly.

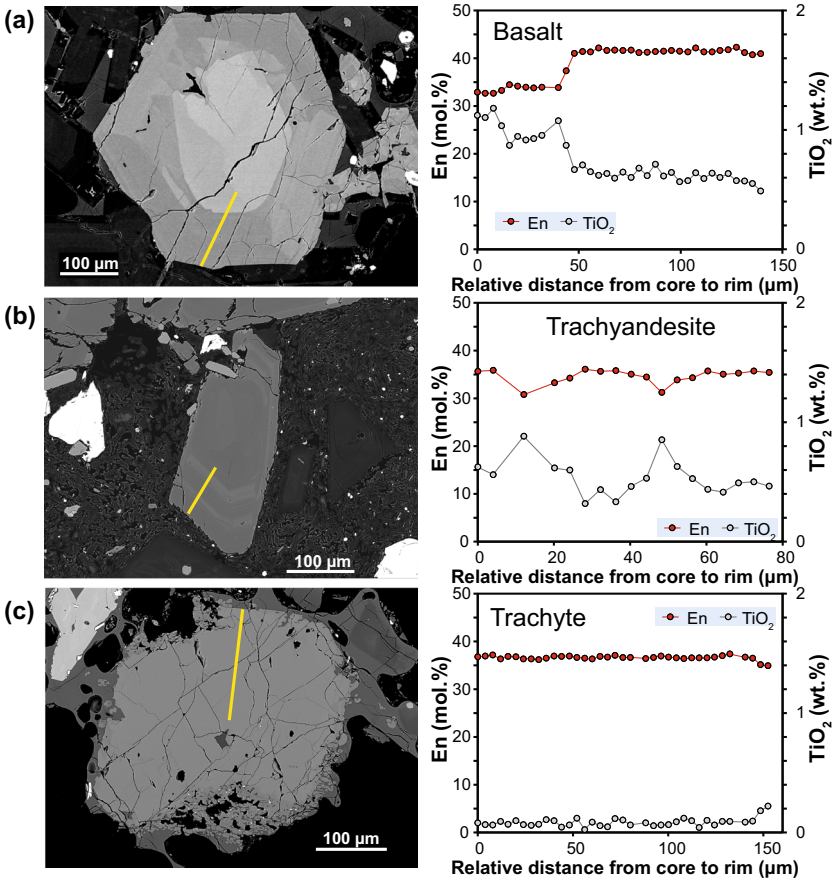

Fig. 10 BSE images and corresponding EPMA transects for representative clinopyroxene phenocrysts from (**a**) basalts, (**b**) trachyandesites, and (**c**) trachytes

Discussion

Basalt petrogenesis

Trace element ratios of Bogoslof basalts suggest a deeper mantle origin than at nearby arc front volcanoes, consistent with its backarc setting. Specifically, we use the approach of Turner et al. (2003) and Jicha et al. (2009), where Tb/Yb ratios estimate the amount of residual garnet, and, coupled with La/Yb, the degree of partial melting. This approach assumes that residual garnet will strongly retain heavy rare earth elements like Yb relative to Tb. Mafic lavas filtered to SiO_2 < 52 wt% from Okmok (Nye and Reid 1986; Finney et al. 2008; Nye et al. 2018) and Makushin (Nye et al. 1986; McConnell et al. 1998; Bean 1999) are consistent with an enriched mantle source with no residual garnet and 5–10% partial melting (Fig. 12). Assuming a more depleted source would result in up to a few percent residual garnet and a similar percent melting. Bogoslof basalt compositions, however, plot with 3–5% residual garnet, assuming an enriched mantle source, and 2–5% partial melting. Thus, the trace element character of Bogoslof basalts suggests that their mantle source likely had more residual garnet and resulted from lower degrees of partial melting than basalts from nearby main arc axis volcanos. In other locations, such as in the Western Aleutians, residual garnet signature has been attributed to contribution from slab melting in the ecologite facies (Yogodzinski et al. 2015). While we do not rule out a role for slab melting, the backarc setting and increased slab depth at Bogoslof is easily explained by higher pressure back-arc mantle melts.

Heterogeneity of matrix glass compositions, especially K_2O (Fig. 5), require some diversity in basaltic inputs. Specifically, microlite-free matrix glass from a quenched and glassy mafic inclusion (18CW100-13B, Fig. 2f) has lower SiO_2 and higher MgO than the host sample matrix glass, consistent with a more primitive magma composition (Fig. 5). The K_2O concentrations, however, are higher in the otherwise primitive inclusion, despite the lack of K-bearing phases in phenocrysts or groundmass of either sample. These differences in K_2O, which are more broadly expressed by a scatter of matrix glass K_2O in tephra samples, are best explained by a diversity of basalt compositions. This diversity could be derived from either separate mantle inputs, suggested by two distinct periods of deep seismic activity during the eruption (Wech et al. 2018), or from some mixing with residual basalts from the 1992 eruption.

Amphibole-bearing basalt was the primary juvenile component of the 2016–2017 eruption (Fig. 3), and apart from the

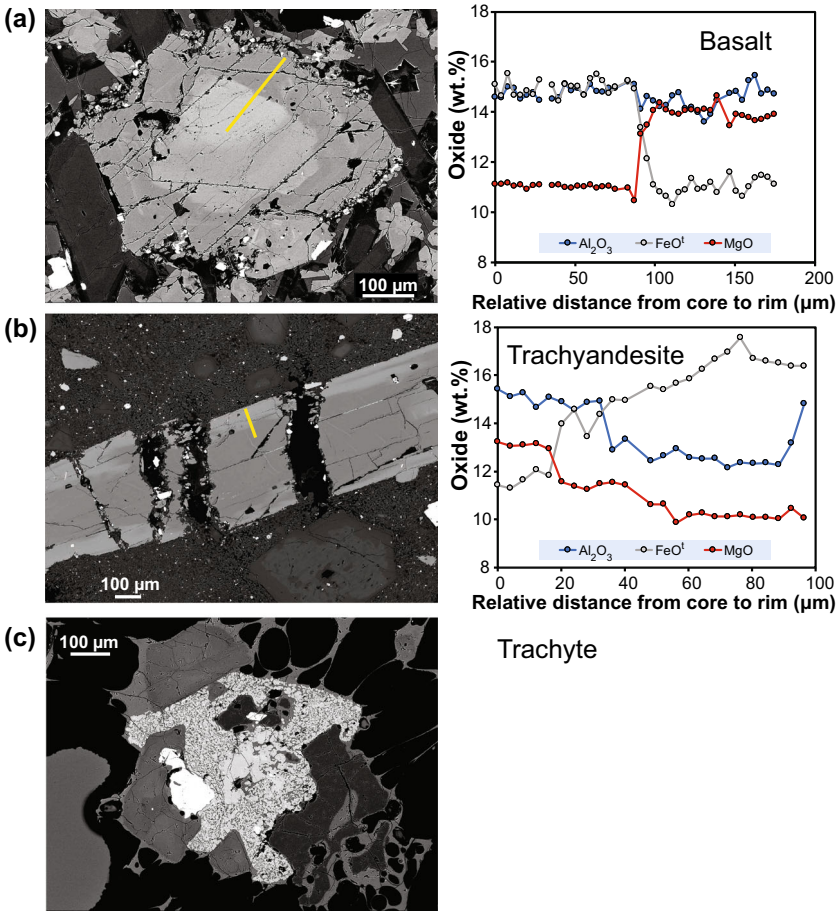

Fig. 11 BSE images and corresponding EPMA transects for representative amphibole phenocrysts from (**a**) basalts, (**b**) trachyandesites, as well as (**c**) a BSE image of amphibole pseudomorph from trachytes (note, the unaltered core material is clinopyroxene, no compositional analyses are shown since unaltered amphibole is not present)

1796 Castle Rock dome, is similar in composition to all other sampled historical eruptive products (Byers 1961). Major-element projections of matrix glass compositions through the bulk basalt composition suggest crystallization of near equal proportions of plagioclase, clinopyroxene, and amphibole (Fig. 5), consistent with the observed phenocryst mineralogy (Fig. 2). While matrix glasses are influenced by both phenocryst and shallow microlite crystallization, the overall similarity of matrix glasses and phenocryst-hosted melt inclusions requires a similar mineral assemblage controlling compositions during phenocryst growth (Fig. 8).

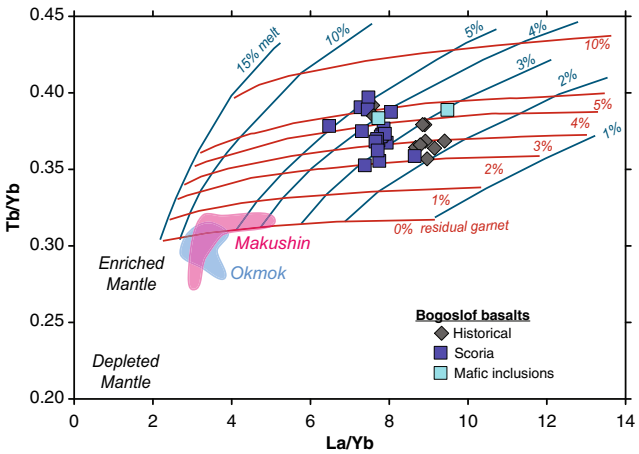

Fig. 12 Trace element ratios in basalt samples (48–52 wt% SiO_2) may indicate degree of partial melting and residual minerals in the mantle source, here with Tb/Yb vs. La/Yb following Turner et al. (2003) and Jicha et al. (2009). Residual garnet and degree of partial melt shown for an enriched mantle source (see Jicha et al. 2009 for calculations). Compositional fields for arc-front volcanos Okmok and Makushin shown for comparison (see Fig. 4 references).

While no exact compositional match exists in experimental literature for Bogoslof basalt, Barclay and Carmichael (2004) provide a useful set of experiments on roughly similar amphibole basalts from central Mexico (their starting material had notably higher Na_2O, K_2O, and included olivine phenocrysts, unlike Bogoslof). In their work, a plagioclase and amphibole mineral assemblage is only stable at low pressures, water contents < 3 wt%, and a relatively narrow 950–1000 °C temperature range. This mineral assemblage was also only achieved at high crystallinities > 50% (Fig. 13). Bogoslof basalts also have > 50% crystallinity, and preliminary melt inclusion water analyses are all < 3.5 wt%. Thus, Bogoslof basalts, matrix glasses, and melt inclusions, are all consistent with shallow pre-eruptive storage of magmas. This phase diagram also illustrates that all erupted Bogoslof basalts are relatively evolved from primary mantle melts due to the absence of

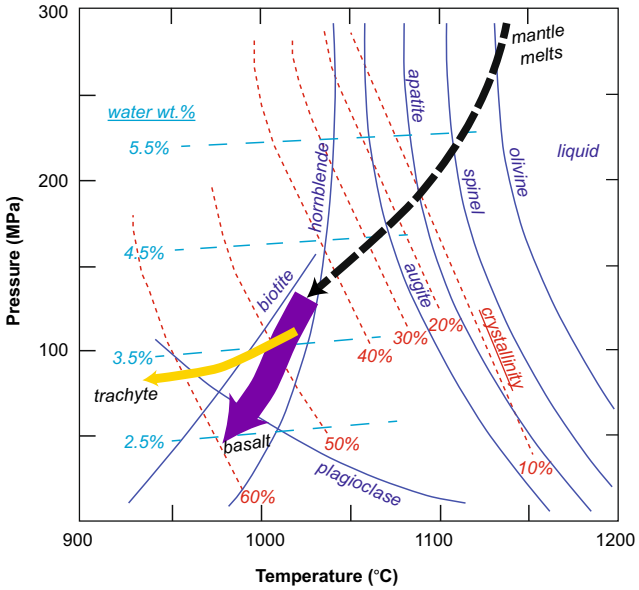

Fig. 13 Experimental phase diagram of Barclay and Carmichael (2004) determined on an alkalic amphibole basalt in Central Mexico. Saturated water concentrations are shown in blue and percent crystals in red. Bogoslof basalt mineralogy (plagioclase, hornblende, clinopyroxene) can only be found < 3 wt% water, 950–1000 °C, and shallow pressures (thick purple arrow). These compositions should be very crystal rich (~ 60%) matching observed crystallinity at Bogoslof. Trachyte compositions must be generated at higher pressure and water concentrations to evolve melt without plagioclase crystallization (yellow arrow). Dashed black arrow indicates that all observed compositions are relatively evolved from primary mantle melts (that would plot off this diagram)

olivine, which must have crystallized earlier in overall magmatic history driving MgO and Ni to lower concentrations observed in all erupted samples at Bogoslof.

The highly microlitic and diktytaxitic textures in 85–90% of basaltic tephra grains (Fig. 3) are typical of dome or cryptodome eruptive products which are dominated by slow magma ascent and shallow pre-eruptive storage (Gaunt et al. 2016; Kushnir et al. 2016). Large amphibole reaction rims also support this conclusion (Rutherford and Hill 1993). High overall phenocryst crystallinity > 50% suggests that despite their mafic composition, the Bogoslof basalts were highly viscous and at threshold of eruptible magmas (Marsh 1981). This high crystallinity could limit potential magma ascent rates and promote effusion as lava domes or as shallow cryptodomes.

Trachyte pumice petrogenesis

Textural and chemical characterization of the trachyte pumice is consistent with a rejuvenated magma similar to the 1796 Castle Rock dome composition. The major and trace element trachyte pumice compositions overlap Castle Rock dome samples, but range to higher SiO_2 following a mostly plagioclase control-line and cross the tholeiitic-calc-alkaline divide (Figs. 4, 5, and 6).

Measured crystallinity of 90% relative to the melt proportion in the trachyte pumice requires an origin from a nearly solid source material that would not be mobile as a fluid (Marsh 1981). In addition, sanidine and plagioclase feldspar, as well as trace quartz, suggest low-temperature eutectic crystallization. Lower temperature accessory minerals like titanite are also present. Feldspars are strongly zoned, with high An cores similar to basalts but with albitic to anorthoclase composition rims (Fig. 9).

Despite the overall high crystal percentage, trachyte groundmass is a microlite-free glass. The average glass composition is in line with the trend of bulk rock values but scattered in a trend perpendicular to the bulk trend with a vector best explained by late melting or crystallization of sanidine (Fig. 5). High 950–1050 °C temperatures calculated from equilibrium pairs of magnetite-ilmenite (see online Supplementary Material) match expected values in amphibole-plagioclase basalts (Fig. 13). Finally, some pumice hand-samples are coated in a mafic rind (Fig. 2b), and other samples have pumice mingled with basaltic scoriacious material. These high estimated temperatures, glassy matrix in an otherwise highly crystalline rock, and occurrence of mafic coatings on pumice can be explained by entrainment of trachyte material into basaltic magmas where they are rapidly heated resulting in small amounts of melt and inflation of residual volatiles.

Since we did not observe any trachyte grains in January, March, or May distal ashfall samples, the pumice likely was only erupted during the end of the 2016–2017 Bogoslof eruption. This fits a magma rejuvenation model, where residual or subsolidus trachyte from the 1796 eruption was heated over the course of the 2016–2017 eruption, and in the final months of the eruption began mingling with the basalt magmas.

The bulk trachyte composition cannot be generated from the shallow liquid line of decent indicated by basalt matrix glass compositions (Fig. 5). Rather, the trachyte composition is consistent with a stronger amphibole influence on overall differentiation. Strongly linear and decreasing Dy/Yb vs. SiO_2 supports amphibole control (Fig. 6). While Eu anomalies are largely absent (Fig. 7), Sr ratioed against elements with similar incompatibility in amphibole, (e.g., Sr/Y, Sr/Zr, Sr/Ba), suggest a significant role for plagioclase in the bulk chemical evolution (Fig. 6). Subtle offset in a linear fit of trachyte to basalt compositions project to slightly higher Al_2O_3 and lower MgO than amphibole and/or clinopyroxene compositions can explain. Thus, trachyte evolution from basalts, if related, require a stronger influence of amphibole than expected from shallow basalts, with a subordinate role for plagioclase.

A two-stage crystallization model could help explain generation of trachyte compositions from basalts, with initial higher-pressure crystallization of amphibole ± clinopyroxene, followed by shallow plagioclase + amphibole + clinopyroxene

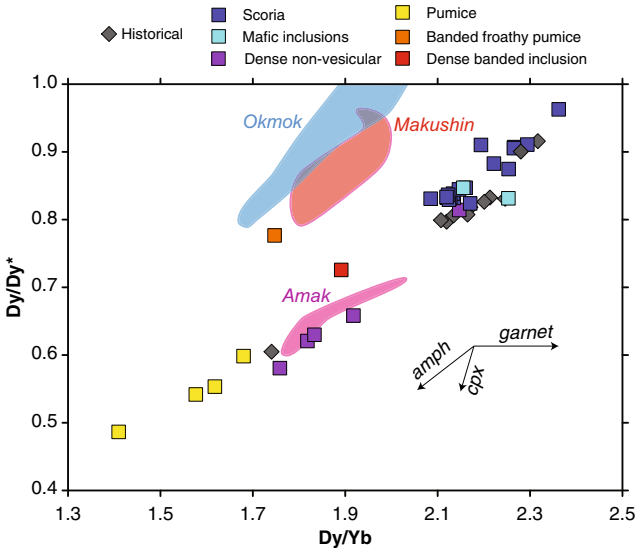

Fig. 14 Dy/Dy* following Davidson et al. (2013), vs. Dy/Yb to differentiate garnet, amphibole, and clinopyroxene crystallization vectors. Bogoslof samples, along with nearby arc-front volcanos, exhibit strong amphibole compositional control, although amphibole phenocrysts are only common at Bogoslof. See Fig. 4 references for Okmok and Makushin data

crystallization seen in basalt matrix glasses (following Barclay and Carmichael 2004 phase relationships, Fig. 13). Elements more strongly influenced by feldspar, such as Sr and Al_2O_3, have a slightly curved evolution supporting such a model.

Davidson et al. (2007) proposed that a zone of amphibole crystallization and accumulation in the mid-crust influences the rare earth element character of many arc rock compositions, regardless of the presence or absence of amphibole phenocrysts in erupted lavas. Bogoslof lavas, where amphibole is clearly present, exhibit a strong Dy/Dy* trend following Davidson et al. (2013), that is also exhibited in nearby Okmok and Makushin lavas where amphibole is absent (Fig. 14). A higher pressure setting in the mid-crust is consistent with expected crystallization sequences for amphibole basalts, however, high crystallinities may make extraction of these magmas exceedingly rare (Barclay and Carmichael 2004).

Intermediate trachyandesites and the December 2016 uplift

Samples of the dome-like outcrop of the December 2016 uplifted area are likely older Bogoslof lavas that were pushed up during shallow 2016–2017 basalt cryptodome emplacement that began in December and continued throughout much of the eruption (Fig. 15). No thermal anomalies were associated with the onset of uplift, which was initially interpreted as a tuff ring (Waythomas et al. 2019b). All explosive events from December to August, and two short-lived subaerial lava

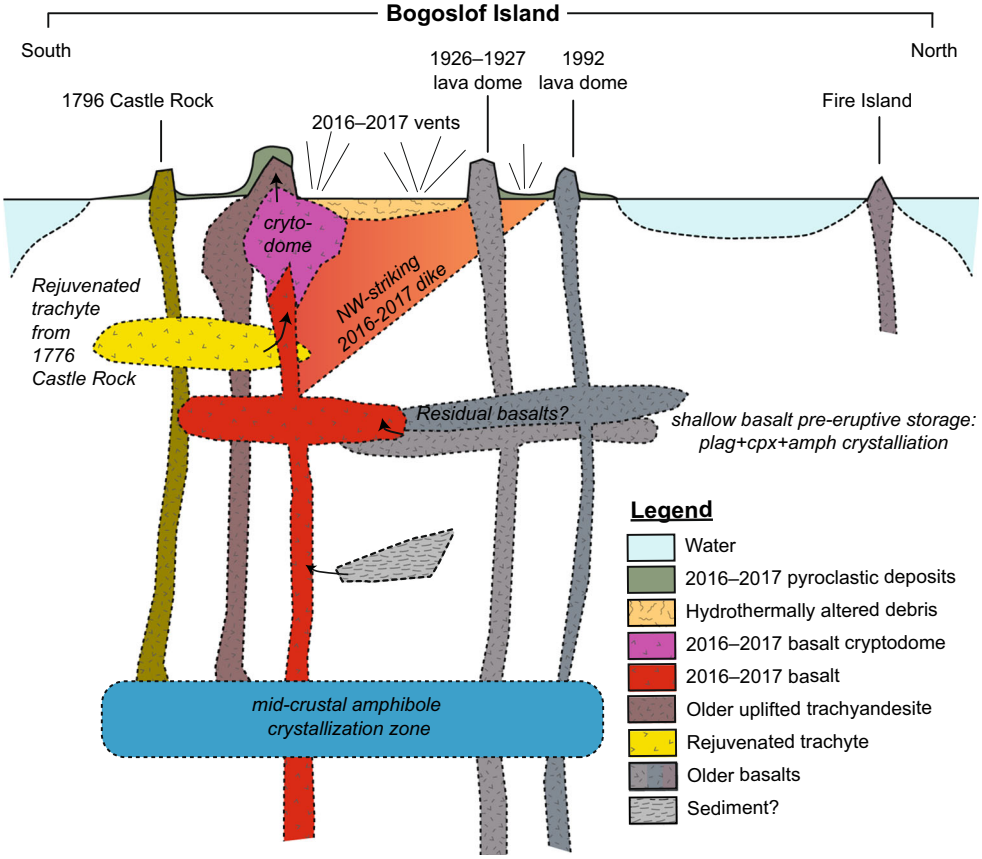

Fig. 15 Conceptual cross-section cartoon of Bogoslof erupted components. Note, evolved magma components such as the trachyte and trachyandesite were likely generated in a deeper storage zone with a stronger influence of amphibole crystallization, while shallow pre-eruptive differentiation occurred with amphibole, plagioclase, and clinopyroxene. Diversity in the 2016–2017 eruption can be achieved through rejuvenation of older magmas such as the 1992 basalt and 1796 trachyte (shown here), or simultaneous intrusion of new magmas from depth. We show a cryptodome of 2016–2017 basalt responsible for uplift of older trachyandesite starting in December 2016. Explosive vents, and possible submarine domes, cryptodomes, and two subaerial domes erupted along a NW-striking dike. Figure is schematic and not drawn to scale

domes in June and August 2017, were to the north of this uplifted area (Waythomas et al. 2019a).

The trachyandesite composition of rocks collected from the base of the uplifted dome, and as ballistics scattered across the island in August 2018, are a unique composition from the basalts and trachyte pumice and are the only erupted material with sanidine-plagioclase-cristobalite groundmass mineralogy (Fig. 2). Tephra samples sometimes have identical feldspar-cristobalite matrix as fresh proximal samples, but also often also include clay-like mineral compositions of feathery crystalline growths that could be a result of hydrothermal alteration and/or glass devitrification (Fig. 3). No glass has been observed associated with the trachyandesite groundmass mineralogy in the freshest proximal material or in any distal tephra grains. All textural indications, along with a lack of thermal anomalies during initial uplift of the material, indicate that the trachyandesite was an older lava or shallow intrusion at the start of the 2016–2017 eruption. Decreasing abundance of this composition in tephra samples from January to May are also consistent with clearing of this material from the vent(s) during explosive activity.

The trachyandesite is the only material with sanidine microlites, yet it lacks the larger sanidine and biotite phenocrysts seen in the trachyte pumice. Higher La/Yb in the trachyandesite than either basalts or trachytes precludes this as a compositional mixture between these endmembers. Rather, the trachyandesite likely represents a separate batch of magma similar to the trachyte composition and not exposed at the surface until uplift during emplacement of a likely basalt cryptodome in December 2016. This composition is unique from any analyzed historical compositions that we have analyzed or is published for Bogoslof (Byers 1961; Arculus et al. 1977) and may represent the oldest lavas now exposed on Bogoslof.

Inclusions

The origin and significance of the abundant mafic and silicic inclusions are beyond the scope of this paper, but worth a brief consideration. As previously discussed, a single separated quenched mafic inclusion has provided evidence for some diversity in basaltic input into the 2016–2017 eruption. One somewhat speculative possibility is that some mafic diversity could result from mixing with a shallow residual magma body from the 1992 and/or earlier eruptions. The large amphibole gabbro likely represents an older crystallized magma intrusion that has since undergone moderate alteration with calcite mineralization.

Layered silicic inclusions are some of the most interesting eruptive products. High vesicularity and glassy groundmass suggests these were melted during the eruption. Their chemistry is dacitic to rhyolitic (Fig. 4) suggesting an evolved composition, but high MgO and FeO concentrations are unusual for such evolved silicic rocks. In addition, incompatible trace element concentrations are unusually low for an evolved rhyolite (Figs. 6 and 7). One possible origin for these inclusions is entrainment of seafloor sediments as magma passes through the oceanic crust at the base of the Bogoslof edifice (Fig. 15). A mixture of terrigenous clays with diatoms could explain the high silica, low incompatible elements, but high Mg and Fe concentrations. Future isotopic work could easily support or invalidate this hypothesis.

Conclusions

The dominant juvenile magmatic component of the 2016–2017 eruption of Bogoslof was a crystal-rich amphibole basalt. Trace element abundances suggest that their mantle source likely had more residual garnet and resulted from lower degrees of partial melting than nearby arc-front volcanoes. The > 50% crystallinity of basalt increased magma viscosity, resulting in a slow overall ascent rate, shallow cryptodome intrusion, and two subaerial domes, all along a NW-trending strike possibly reflecting a dike source (Waythomas et al. 2019b; Fig. 15). An early cryptodome uplifted and exposed older trachyandesite lava that was incorporated as non-juvenile lithics into erupted tephras. Late in the eruption, evolved trachyte, possibly rejuvenated from a 1796 magma, was incorporated into the basalt.

While shallow submarine eruptions have enhanced explosivity from the involvement of external water, characterized by the iconic 1963–1964 eruption of Surtsey, Iceland, shallow submarine dome eruptions are not well-described (White and Houghton 2000; White et al. 2015). In the case of Bogoslof, eruptive products available at this time are indistinguishable from typical vulcanian eruptions of lava domes and cryptodomes. External water was clearly a factor in water-rich eruption plumes (Schneider et al. 2019) and proximal tuff-ring and dune deposits (Waythomas et al. 2019b). In addition, overlying water may have aided in the quenching of a cryptodome or submarine dome carapace, allowing for the large volatile buildup and release as large bubble-forming gas slugs at the surface preceding many explosive events (Lyons et al. 2019b).

More work is needed to understand this rare volcanic eruption style and setting. Further physical characterization of tephra deposits may help define the role, or lack of role, for external water in triggering and enhancing explosive events. More in-depth examination of the geochemistry will provide a rare insight into back arc magma genesis in the Aleutians. While Bogoslof is a unique volcano in its setting and erupted composition, it may

also provide insight into the magmatic source of cryptic amphibole signatures seen in arcs worldwide.

Acknowledgments Sample preparation and some SEM imaging assistance was provided by Fiona Eberhardt. The crew of the U.S. Fish and Wildlife Service R/V Tiglax helped with field and logistical support to collect 2018 samples. The manuscript was developed and improved especially by discussions with Tom Sisson, Alexa Van Eaton, and Heather Wright, as well as constructive reviews by Dawnika Blatter, an anonymous reviewer, and editorial handling by John Lyons. Funding for this study was provided by the U.S. Geological Survey Volcano Hazards Program. Any use of trade, firm, or product names is for descriptive purposes only and does not imply endorsement by the U.S. Government.

References

Arculus RJ, Delong SE, Kay RW, Brooks C, Sun SS (1977) The alkalic rock suite of Bogoslof Island, Eastern Aleutian Arc, Alaska. J Geol 85:177–186. https://doi.org/10.1086/628284

Arculus RJ, Johnson RW, Chappell BW, McKee CO, Sakai H (1983) Ophiolite-contaminated andesites, trachybasalts, and cognate inclusions of Mount Lamington, Papua New Guinea: anhydrite-amphibole-bearing lavas and the 1951 cumulodome. J Volcanol Geotherm Res 18:215–247. https://doi.org/10.1016/0377-0273(83)90010-0

Bacon CR, Hirschmann MM (1988) Mg/Mn partitioning as a test for equilibrium between coexisting Fe-Ti oxides. Am Mineral 73:57–61

Barclay J, Carmichael IS (2004) A hornblende basalt from Western Mexico: water-saturated phase relations constrain a pressure-temperature window of eruptibility. J Petrol 45:485–506. https://doi.org/10.1093/petrology/egg091

Bean KW (1999) The Holocene eruptive history of Makushin Volcano, Alaska. Dissertation, University of Alaska, Fairbanks.

Byers FM (1961) Petrology of three volcanic suites, Umnak and Bogoslof Islands, Aleutian Islands, Alaska. Geol Soc Am Bull 72:93–128. https://doi.org/10.1130/0016-7606(1961)72[93:POTVSU]2.0.CO;2

Coombs ML, Wech A, Haney M, Lyons J, Schneider DJ, Schwaiger H, Wallace K, Fee D, Freymueller J, Schaefer J (2018) Short-term forecasting and detection of explosions during the 2016–2017 eruption of Bogoslof volcano, Alaska. Front Earth Sci 6:122

Coombs M, Wallace K, Cameron C, Lyons J, Wech A, Angeli K, Cervelli P (2019) Overview, chronology, and impacts of the 2016–2017 eruption of Bogoslof volcano, Alaska. Bull Volcanol 81:62. https://doi.org/10.1007/s00445-019-1322-9

Davidson J, Turner S, Handley H, Macpherson CG, Dosseto A (2007) Amphibole "sponge" in arc crust? Geology 35:787–790

Davidson J, Turner S, Plank T (2013) Dy/Dy*: variations arising from mantle sources and petrogenetic processes. J Petrol 54:525–537. https://doi.org/10.1093/petrology/egs076

Finney B, Turner S, Hawkesworth C, Larsen J, Nye C, George R, Bindeman I, Eichelberger J (2008) Magmatic differentiation at an island-arc caldera: Okmok Volcano, Aleutian Islands, Alaska. J Petrol 49:857–884. https://doi.org/10.1093/petrology/egn008

Gaunt HE, Bernard B, Hidalgo S, Proaño A, Wright H, Mothes P, Criollo E, Kueppers U (2016) Juvenile magma recognition and eruptive dynamics inferred from the analysis of ash time series: The 2015 reawakening of Cotopaxi volcano. J Volcanol Geotherm Res 328:134–146. https://doi.org/10.1016/j.jvolgeores.2016.10.013

Ghiorso MS, Evans BW (2008) Thermodynamics of rhombohedral oxide solid solutions and a revision of the Fe-Ti two-oxide geothermometer and oxygen-barometer. Am J Sci 308:957–1039

Jicha BR, Hart GL, Johnson CM, Hildreth W, Beard BL, Shirey SB, Valley JW (2009) Isotopic and trace element constraints on the petrogenesis of lavas from the Mount Adams volcanic field, Washington. Contrib Mineral Petrol 157:189–207. https://doi.org/10.1007/s00410-008-0329-6

Johnson DM, Hooper PR, Conrey RM (1999) XRF analysis of rocks and minerals for major and trace elements on a single low dilution Li-tetraborate fused bead. Adv X-ray Anal 41:843–867

Kushnir ARL, Martel C, Bourdier JL, Heap MJ, Reuschlé T, Erdmann S, Komorowski J, Cholik N (2016) Probing permeability and microstructure: Unravelling the role of a low-permeability dome on the explosivity of Merapi (Indonesia). J Volcanol Geotherm Res 316:56–71. https://doi.org/10.1016/j.jvolgeores.2016.02.012

Le Maitre RW, Bateman P, Dudek A, Keller J, Lameyre Le Bas MJ, Sabine PA, Schmid R, Sorensen H, Streckeisen A, Wooley AR, Xanettin B (1989) A classification of igneous rock and glossary of terms. Blackwell, Oxford

Lopez T, Clarisse L, Schwaiger H, Van Eaton A, Loewen M, Fee D, Lyons J, Wallace K, Searcy C, Wech A, Haney M, Schneider D, Graham N (2019) Constraints on eruption processes and event masses for the 2016–2017 eruption of Bogoslof volcano, Alaska, through evaluation of IASI satellite SO_2 masses and complementary datasets. Bull Volcanol (part of the Bogoslof Topical Collection)

Lowenstern JB, Pitcher BW (2013) Analysis of H_2O in silicate glass using attenuated total reflectance (ATR) micro-FTIR spectroscopy. Am Mineral 98:1660–1668. https://doi.org/10.2138/am.2013.4466

Luhr JF, Carmichael ISE (1985) Jorullo Volcano, Michoacán, Mexico (1759–1774): The earliest stages of fractionation in calc-alkaline magmas. Contrib Mineral Petrol 90:142–161. https://doi.org/10.1007/BF00378256

Lyons JJ, Iezzi AM, Fee D, Schwaiger HF, Wech AG, Haney MM (2019a) Infrasound generated by the shallow submarine eruption of Bogoslof volcano, Alaska. Bull Volcanol (part of the Bogoslof Topical Collection)

Lyons JJ, Haney MM, Fee D, Wech AG, Waythomas CF (2019b) Infrasound from giant bubbles during explosive submarine eruptions. Nat Geosci 12: 952–958. https://doi.org/10.1038/s41561-019-0461-0

Marsh BD (1981) On the crystallinity, probability of occurrence, and rheology of lava and magma. Contrib Mineral Petrol 78:85–98

Marsh BD, Leitz RE (1978) Geology of Amak Island, Aleutian Islands, Alaska. J Geol 87:715–723. https://doi.org/10.1086/628461

McConnell VS, Beget JE, Roach AL, Bean KW, Nye CJ (1998) Geologic map of the Makushin volcanic field, Unalaska Island, Alaska. Alaska Division of Geological & Geophysical Surveys Report of Investigation 97-20, unpaged, 2 sheets, scale 1:63,360.

Miyashiro A (1974) Volcanic rock series in island arcs and active continental margins. Am J Sci 274:321–355

Nielsen CH, Sigurdsson H (1981) Quantitative methods for electron micro-probe analysis of sodium in natural and synthetic glasses. Am Mineral 66:547–552

Nye CJ, Reid MR (1986) Geochemistry of primary and least fractionated lavas from Okmok volcano, Central Aleutians: implications for arc magmagenesis. J Geophys Res 9:10,271–10,287

Nye CJ, Swanson SE, Reeder JW (1986) Petrology and geochemistry of Quaternary volcanic rocks from Makushin volcano, central Aleutian Arc. Alaska Division of Geological & Geophysical Surveys Public-Data File 86-80: 123 p., 1 sheet, scale 1:50,000.

Nye CJ, Beget JE, Layer PW, Mangan MT, McConnell VS, McGimsey RG, Miller TP, Moore RB, Stelling PL (2018) Geochemistry of some quaternary lavas from the Aleutian Arc and Mt. Wrangell.

Alaska Division of Geological & Geophysical Surveys Raw Data File 2018: 1-29 p. https://doi.org/10.14509/29843

Rutherford MJ, Hill P (1993) Magma ascent rates from amphibole breakdown: an experimental study applied to the 1980–1986 Mount St. Helens eruptions. J Geophys Res 98:19667–19685

Schneider DJ, Van Eaton AR, Wallace KL (2019) Satellite observations of the 2016–17 eruption of Bogoslof volcano: aviation and ash fallout hazard implications from a water-rich eruption. Bull Volcanol (part of the Bogoslof Topical Collection)

Searcy CK, Power JA (2019) Seismic character and progression of explosive activity during the 2016–2017 eruption of Bogoslof volcano, Alaska. Bull Volcanol. https://doi.org/10.1007/s00445-019-1343-4

Sigurdsson H, Shepherd JB (1974) Amphibole-bearing basalts from the submarine volcano Kick'em-Jenny in the Lesser Antilles island arc. Bull Volcanol 38:891. https://doi.org/10.1007/BF02597097

Tepp G, Dziak R, Haney M, Lyons J, Searcy C, Matsumoto H, Haxel J (2019) Seismic and hydroacoustic observations of the 2016–17 Bogoslof Eruption. Bull Volcanol. https://doi.org/10.1007/s00445-019-1344-3

Turner S, Foden J, George R, Evans P, Varne R, Elburg M, Jenner G (2003) Rates and processes of potassic magma evolution beneath Sangeang Api volcano, east Sunda arc, Indonesia. J Petrol 44:491–515. https://doi.org/10.1093/petrology/44.3.491

Van Eaton AR, Schneider DJ, Smith CM, Haney MM, Lyons JJ, Said R, Fee D, Holzworth RH, Mastin LG (2019) Did ice-charging generate volcanic lightning during the 2016–2017 eruption of Bogoslof volcano, Alaska? Bull Volcanol (part of the Bogoslof Topical Collection)

Waters LE, Cottrell E, Kelly K, Coombs ML (2017) Calc-alkaline liquid lines of descent produced under oxidizing conditions: an experimental and petrologic study of basaltic tephras from the Western Aleutians, AK. Abstract V11B-0343 presented at 2017 AGU Fall Meeting, New Orleans, LA, 11-15 Dec.

Waythomas CF, Cameron CE (2018) Historical eruptions and hazards at Bogoslof Volcano, Alaska. U.S. Geol Surv Sci Investig Rep 2018-5085:1–54

Waythomas CF, Angeli K, Wessels RL (2019a) Evolution of the submarine-subaerial edifice of Bogoslof volcano, Alaska, during its 2016–2017 eruption based on analysis of satellite imagery. Bull Volcanol (part of the Bogoslof Topical Collection)

Waythomas CF, Loewen MW, Wallace KL, Cameron CE, Larsen JF (2019b) Geology and eruptive history of Bogoslof volcano. Bull Volcanol (part of the Bogoslof Topical Collection)

Wech A, Tepp G, Lyons J, Haney M (2018) Using earthquakes, T waves, and infrasound to investigate the eruption of Bogoslof Volcano, Alaska. Geophys Res Lett 45:6918–6925. https://doi.org/10.1029/2018GL078457

White J, Houghton B (2000) Surtseyan and related phreatomagmatic eruptions. In: Sigurdsson H, Houghton B, Rymer H, Stix J, McNutt S (eds) , 1st edn. Academic Press, Encyclopedia of volcanoes, pp 495–511

White J, Schipper C, Kano K (2015) Submarine explosive eruptions. In: Sigurdsson H, Houghton B, McNutt S, Rymer H, Stix J (eds) Encyclopedia of volcanoes, 2nd edn. Academic Press, pp 553–569

Yogodzinski GM, Brown ST, Kelemen PB, Vervoort JD, Portnyagin M, Sims KWW, Hoernle K, Jicha BR, Werner R (2015) The role of subducted basalt in the source of island arc magmas: evidence from seafloor lavas of the Western Aleutians. J Petrol 56:441–492. https://doi.org/10.1093/petrology/egv006